# Passive Superconducting Circulator on a Chip

Rohit Navarathna,[1,*] Dat Thanh Le,[1] Andrés Rosario Hamann,[1,†] Hien Duy Nguyen,[2]
Thomas M. Stace,[1,3] and Arkady Fedorov[1,3,‡]
[1]*ARC Centre for Engineered Quantum System, School of Mathematics and Physics, University of Queensland, Brisbane QLD 4072, Australia*
[2]*School of Mathematics and Physics, University of Queensland, Brisbane QLD 4072, Australia*
[3]*Analog Quantum Circuits Pty. Ltd., Brisbane QLD 4072, Australia*

(Received 26 September 2022; accepted 3 January 2023; published 20 January 2023)

An on-chip microwave circulator that is compatible with superconducting devices is a key element for scale up of superconducting circuits. Previous approaches to integrating circulators on chip involve either external driving that requires extra microwave lines or a strong magnetic field that would compromise superconductivity. Here we report the first proof-of-principle realization of a passive on-chip circulator that is made from a superconducting loop interrupted by three notionally identical Josephson junctions and is tuned with only dc control fields. Our experimental results show evidence for nonreciprocal scattering, and excellent agreement with theoretical simulations. We also present a detailed analysis of quasiparticle tunneling in our device using a hidden Markov model. By reducing the junction asymmetry and utilizing the known methods of protection from quasiparticles, we anticipate that Josephson-loop circulator will become ubiquitous in superconducting circuits.

DOI: 10.1103/PhysRevLett.130.037001

Circulators, nonreciprocal devices that route signals and isolate devices from noise, are a crucial component in cryogenic environments such as superconducting circuits [1,2]. When used as isolators, they typically route the low power signals from a quantum system to an amplifier, while redirecting noise from the amplifier to a matched load, thus protecting the coherence of the quantum system [3,4]. Circulators can also function as duplexers that separate the input and output signals to and from a device [5]. This is particularly useful for reflection measurements, where the outgoing signal needs to be separated from the incoming one.

Most commercial microwave circulators harness ferrite components and the Faraday effect to achieve nonreciprocity [1,6], which presents bottlenecks for future development of large-scale superconducting quantum processors. First, they are microwave-interference devices, so their size is set by the microwave wavelength. Second, the ferrite materials make it impractical to integrate them on a nanofabricated microwave chip. Furthermore, losses at the cable interconnections for cascaded circulators reduce the quantum efficiency of measurement and control at the quantum noise limit.

Various approaches to miniaturising circulators have been proposed. Some involve driven elements to induce symmetry-breaking fields that require active microwave control lines and consume additional energy [3,13–23]. Others nonreciprocal devices exploit the quantum Hall effect in a two-dimensional gas that necessitates very large magnetic fields [24–26] which are detrimental to superconducting circuits. Recently, a different method exploiting the idea of the giant atom in Waveguide QED to make a passive circulator has been proposed [27]. In this Letter, we present the first implementation of an on-chip circulator which is both passive and compatible with superconducting circuits. Our design is based on a superconducting ring interrupted by three Josephson junctions, which forms three superconducting islands that are capacitively coupled to external input-output ports [28,29]. The device is tuned by only dc control fields that include three charge biases to control the charge distribution on the superconducting islands and a small magnetic flux to break time-reversal symmetry. In our system, we use an external bias coil, but the same effect could be provided on-chip with a proximal current bias line. Interference of transitions between the ground state and the excited states of the superconducting ring results in nonreciprocal effects and signal circulation.

Our circulator is schematically displayed as a lumped-element circuit in Fig. 1(a), consisting of a superconducting loop interrupted by three Josephson junctions. This creates three superconducting islands that are capacitively coupled to external 50 Ω microwave lines. These lines are the input or output ports, carrying microwave signals and supplying dc bias voltages $V_i$ $(i = 1, 2, 3)$ to each superconducting island. The superconducting loop is also threaded by an external flux $\Phi$ provided by a coil. The false-color optical microscope image in Fig. 1(b) shows a fabricated sample consistent with the lumped-element model. The sample is made of aluminum deposited on a high-resistivity silicon substrate. It is mounted to the mixing chamber plate of

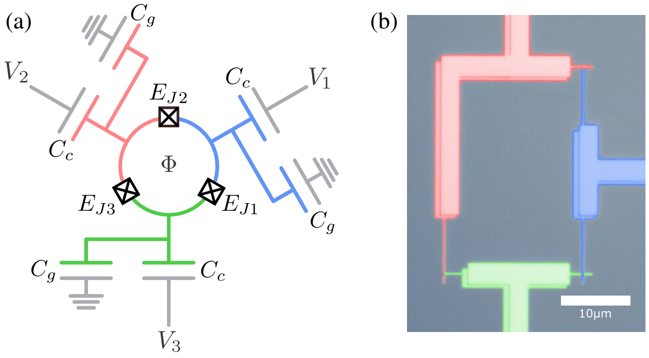

FIG. 1. (a) Lumped-element circuit of the passive on-chip superconducting circulator. The device is a superconducting loop that is interrupted by three Josephson junctions to form three superconducting islands. The islands are biased by three gate charges and coupled to the external ports by interdigitated capacitors. The superconducting loop is threaded by an external flux. (b) False colored optical microscope image of a fabricated loop. The three islands are red, blue, and green. The Josephson junctions are formed by overlapping two layers of aluminium with a layer of aluminium oxide in between.

the dilution refrigerator and connected to three readout chains (see Fig. S1 of the Supplemental Material [7] for details). This facilitates performing simultaneous three-port characterization.

In our device, there are two primary energy scales: the charging energy $E_C$ and the mean Josephson energy $\bar{E}_J$. We chose the values of $E_C$ and $\bar{E}_J$ such that $\bar{E}_J/E_C \sim 2$, which is in between the Cooper-pair box [30] and transmon regimes [31]. This, as pointed out in Ref. [32], helps increase the bandwidth and relax constraints on junction fabrication, while introducing charge noise to the device. We also selected the working frequency of the device to be around 6 GHz, which is within the bandwidth of the amplifiers used in our experiment.

We carried out spectroscopic measurements on the device using two ports of a vector network analyzer (VNA). The source and receiver ports of the VNA were, respectively, connected to one of the input-output microwave cable ports of the device to measure reflection from or transmission through it.

Spectroscopic measurements are shown as a function of the reduced flux $\phi$ in Fig. 2(a) and the charge bias $n_{g1}$ in Fig. 2(b). The density plots are the minimum of 100 reflection measurements at a bandwidth of 15 kHz. This ensures that the transition frequency for each quasiparticle sector was captured in at least one of the 100 measurements. We fit the transition frequencies with the eigenenergies found by solving the eigensystem of the Hamiltonian $\hat{H}$ in Eq. (S1) [7]. This allows us to extract the device parameters; in particular, the fit found the charging energy $E_C/\hbar = 3.98$ GHz and the Josephson energies $E_{Ji}/\hbar = \{7.85, 8.28, 8.55\} \times$ GHz, which yields $\bar{E}_J/E_C \sim 2$ and matches the values from our room-temperature resistance measurements. In Ref. [32], we showed that the tolerable asymmetry of the junctions was 1% or less, which is determined by the requirement that the junction asymmetry is lower than the external coupling bandwidth, which we estimate from Fig. 3 to be $\Gamma \approx 70$ MHz. This is consistent with the predicted bandwidth in [32], given $E_J \approx 8$ GHz. This bandwidth can be improved with better impedance matching, which is the subject of future research.

The half-width of the dispersion in $E_J$ is $\delta E_J = 350$ MHz, so $\delta E_J/\Gamma \approx 5$. Comparing to theoretical results

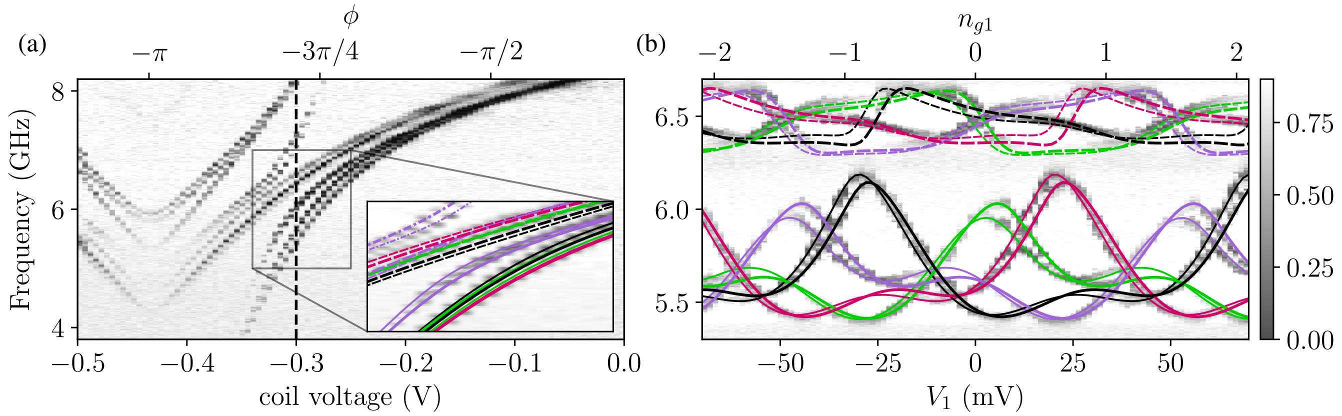

FIG. 2. Reflection measurements from port 1 and fit of the device (a) to an external flux ($\phi$) sweep, (b) to a charge bias ($n_{g1}$) sweep at a coil voltage shown by the black dashed line in (a). The reflection is measured using a vector network analyzer (VNA) with a bandwidth of 15 kHz, allowing the VNA to capture the drop in reflection before a quasiparticle-tunneling event. This measurement is repeated 100 times, and the minimum for each frequency is plotted as the gray scale density plot after background subtraction. The lines in the inset of (a) and in (b) are the transition frequencies fitted to the extracted minima for each frequency. There are four transition frequencies (solid, dashed, dash-dotted, dotted) for each quasiparticle configuration (black, purple, green, magenta) and for two charge configurations (two different line thicknesses). Both fits have the same values of $\{E_C, E_{J1}, E_{J2}, E_{J3}\}/\hbar = \{3.98, 7.85, 8.28, 8.55\} \times$ GHz. We show the full fit for (a) in Fig. S3 of the Supplemental Material [7].

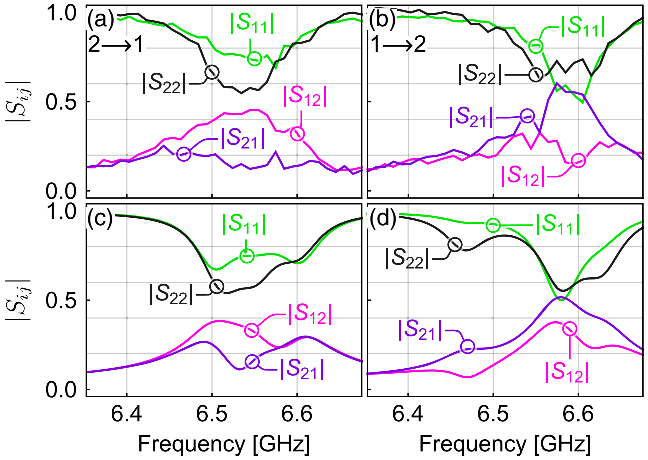

FIG. 3. Experimentally extracted partial $S$-matrix elements for two different charge-bias configurations. In (a) $|S_{12}| > |S_{21}|$, showing that signals are transmitted more from port 2 to port 1 than from 1 to 2. In (b) a different charge-bias configuration yields $|S_{12}| < |S_{21}|$, reversing the nonreciprocity. The full 3-port $S$ matrix is shown in Fig. S3 of the Supplemental Material [7]. (c) and (d) Theoretical simulations corresponding to the experimental configurations above, using the fitting results from Fig. 2 and averaging over the four quasiparticle sectors. We see a good qualitative agreement between experiment and theory.

in [32] [see Fig. 5(b) therein], we see that the circulator fidelity drops below 0.6 for $\delta E_J/\Gamma > 5$, so we conclude the nonreciprocity displayed by the device is limited by the junction asymmetry.

In Fig. 2(a), the transition frequencies are grouped into clusters, each of which contains eight closely located lines. These correspond to two different charge-bias configurations, each consisting of four charge-parity sectors of the superconducting loop [32] that exchange to each other due to intermittent quasiparticle-tunneling events across the islands. The loop is galvanically isolated, so the total loop charge is conserved. The different quasiparticle sectors are represented by the charge parities of two of the superconducting islands, e-e, e-o, o-e, and o-o, where e (o) means an even (odd) number of electrons on a particular island. As shown later, we fit a hidden Markov model to stochastic, experimental time-series data to characterize the populations and lifetimes of the quasiparticle sectors.

In Fig. 2(b), we observed two different spectra that belong to the two different charge-bias configurations. We attribute this to the presence of a charge fluctuator located near the superconducting loop. Using our fit routine, we found that the differences in the charge biases of the two configurations are $\{0.11, -0.03, 0.04\}$, indicating that the charge fluctuator is close to the first superconducting island. Moreover, the transition frequencies in Fig. 2(b) are periodic with $n_{g1}$, as expected for superconducting devices tuned with offset charge biases [30,31]. The periodicity is found to be three Cooper pairs, which is consistent with the fact that there are three superconducting islands in the device. In contrast to the assumption in Ref. [28], we do not observe discontinuities in the spectrum due to changes in the total charge of the three islands.

Besides the mentioned-above fast charge events, we furthermore observed slow charge drift that occurred roughly every 10 min. This set new values for the charge offsets $\mathbf{n}_g$ and resulted in random change in the transition frequencies. An example of this is shown in Fig. S1 of the Supplemental Material [7], where we recorded the minimum amplitude of reflection for 100 frequency sweeps.

Using the four-port VNA and three output readout chains we performed three-port characterization of our device. Specifically, one port of the VNA was used as the source and connected to a mechanical microwave switch to send signals to one of the three input ports. The three readout chains were connected to the other three ports of the VNA, which allows measuring three S parameters, $S_{1j}$, $S_{2j}$, and $S_{3j}$, at the same time, where $j$ is the input port. By switching the input port $j$, we obtained the full $S$ matrix.

Following this procedure, in Fig. 3 we show a part of the experimentally extracted $S$ matrix, which reveals noneciprocity in our device. In Fig. 3(a), we see that when the drive frequency is around 6.5 GHz, $|S_{12}| > |S_{21}|$. At this frequency, the reflections $|S_{11}|$ and $|S_{22}|$ are also at minima. Figure 3(b) shows that by tuning the charge-bias voltages $V_1$, $V_2$, and $V_3$ (at constant flux bias) we can tune the device so that $|S_{12}| < |S_{21}|$; that is, we are able to electronically change the direction of signal transfer. We provide the full $S$ matrix for both circulation directions in Fig. S5 of the Supplemental Material [7].

In Figs. 3(c) and 3(d), we performed simulations to reconstruct the $S$-matrix elements in Figs. 3(a) and 3(b). To this end, we use the device parameters measured in Fig. 2 and for each working point (including the external biases and the signal frequency) we compute the $S$ matrix for all four quasiparticle sectors, and then average over the sectors (with equal weights) to achieve an averaged $S$ matrix. Comparing Figs. 3(a) and 3(b) to Figs. 3(c) and 3(d), respectively, we found qualitative agreement between theory and experiment.

Given the deleterious effect of quasiparticles and junction fabrication asymmetry on circulation, we computed the potential performance of the device in two scenarios that remove these two effects. First, we computed the performance assuming that the system dwells in a single quasiparticle sector. The simulated $S$ matrix for this case is in Fig. 4(a), where we see a much stronger effect on resonance, $S_{11} \ll 1$, but only modest changes in the off-diagonal elements. Second, we compute the performance when reducing the junction asymmetry, in addition to suppressing quasiparticle tunneling. In Fig. 4(b), we show the $S$-matrix elements assuming 1% junction asymmetry, i.e., $E_{J1}/E_{J2} = 0.99$ and $E_{J3}/E_{J2} = 1.01$. From these simulations we estimate the bandwidth within a single quasiparticle sector to be around 70 MHz.

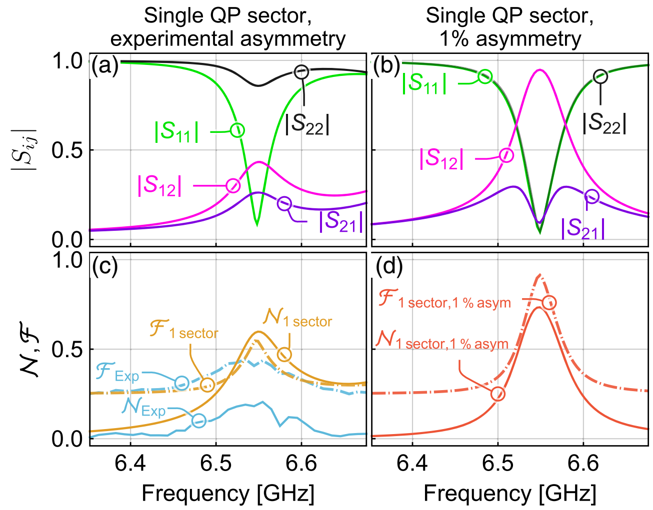

FIG. 4. (a) Simulated $S$-matrix elements when the device stays in a single quasiparticle (QP) sector with the same junction asymmetry as in the current sample. (b) Simulated $S$ matrix with junction asymmetry reduced to 1%, with $E_{J1}/E_{J2} = 0.99$ and $E_{J3}/E_{J2} = 1.01$. (c) Nonreciprocity and fidelity defined in Eqs. (1) and (2) for the experimentally measured $S$ matrix, and for the simulated $S$ matrix with the experimentally determined values of $E_J$ but no QP tunneling. (d) Simulated $S$ matrix with no QP tunneling, and 1% junction dispersion.

To quantify the observed and simulated circulation, we introduce the nonreciprocity, $\mathcal{N}$ [33], and the fidelity, $\mathcal{F}$ [34]

$$\mathcal{N} = \|\mathbf{S} - \mathbf{S}^\intercal\|/\sqrt{8}, \tag{1}$$

$$\mathcal{F} = 1 - \sum_{i,j} ||S_{ij}| - |S_{ij}^{\text{ideal}}||/8, \tag{2}$$

where $\|X\| = \sqrt{\operatorname{Tr}(XX^\dagger)}$ denotes the norm of a matrix $X$, $\sqrt{8}$ is a normalization factor, and $S_{ij}^{\text{ideal}}$ are the elements of an ideal circulator scattering matrix. We comment more on the nonreciprocity measure in Fig. S4 of the Supplemental Material [7].

In Fig. 4(c), we show the nonreciprocity $\mathcal{N}$ for both the experimentally measured $S$ matrix in Fig. 3(a), $\mathcal{N}_{\text{exp}}$, and the "no-quasiparticle-tunneling" $S$ matrix in Fig. 4(a), $\mathcal{N}_{\text{1 sector}}$. We see that the nonreciprocity for the latter is considerably improved, while the fidelities of the two cases, $\mathcal{F}_{\text{exp}}$ and $\mathcal{F}_{\text{1 sector}}$, are comparable, indicating that a higher nonreciprocity is necessary but not sufficient for better circulation.

Reducing the junction asymmetry to 1%, in addition to suppressing quasiparticle tunneling, greatly boosts the device performance. Figure 4(d) shows theoretical predictions for the fidelity and nonreciprocity in the absence of quasiparticle fluctuations, and assuming parameter variations are reduced to 1%. We see both the nonreciprocity and the fidelity are substantially improved relative to the experimental results.

Because of the significant impact of quasiparticle tunneling, we modified the setup to measure the $S$ matrix in 30 μs, faster than the quasiparticle tunneling rate (See Fig. S5 of the Supplemental Material [7] for the measurement schematic). Using a high power of −100 dBm to enhance the single-shot signal-to-noise ratio, we distinguish the distinct states corresponding to four quasiparticle sectors. We employed a hidden Markov model (HMM) to analyze 32 768 time-series measurements of the scattering matrix (see Sec. VII of the Supplemental Material [7] for details) [8–10]. At each time step, the HMM is able to make a statistical inference about the hidden quasiparticle state from the full $3 \times 3$ scattering matrix, and the emission statistics from the data within each hidden state.

In Fig. 5(b), we plot a histogram of $S_{11}$ in the IQ plane which reveals four distinct clusters, one per quasiparticle sector. Figure 5(a) shows the $Q$-quadrature $S_{11}$ switching between the four values, and is associated to one of the four quasiparticle sectors, indicated by the colors.

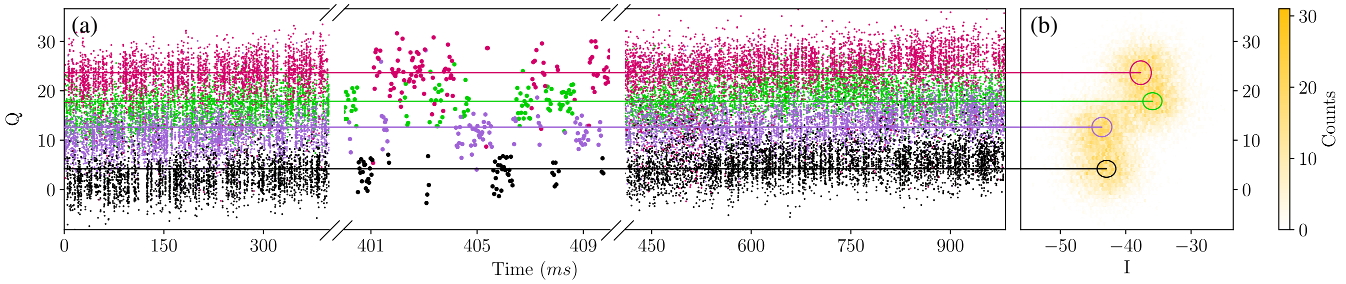

FIG. 5. (a) Repeated measurement of $S_{11}$ of the device at a frequency of 6.709 GHz, an external flux $\phi = 1.9$. The out-of-phase quadrature $Q$ versus time shows Gaussian noise that switches between one of four unobserved states. We fit the full $3 \times 3$ scattering matrix data, $\mathbf{S}$, with a four-state hidden Markov model (HMM), using approximately 32 k time samples, and attribute the data to one of the four hidden states accordingly, indicated by color. We interpret these states as the quasiparticle states seen in Fig. 2. (b) Histogram of the $S_{11}$ data in the IQ plane, showing clustering of $S_{11}$. We also show the $1\sigma$ confidence ellipse extracted from the HMM (circles). We note that the separation in the hidden state data is greater than observed here, which is merely a projection of $\mathbf{S}$ onto a two-dimensional subspace.

The necessary power used to classify the data led to a diminished nonreciprocity for each quasiparticle sector. With quantum limited amplifiers, one could classify the quasiparticle sectors at a lower power. In this case, we expect to see higher circulation for one of the quasiparticle sectors as theoretically estimated in Fig. 4.

Using the HMM, we find that the jumps between the quasiparticle states are well described by Poisson processes with decay times of around 200 μs in each quasiparticle sector (see Fig. S7 of the Supplemental Material [7]).

Postfabrication laser annealing has been shown to retune the variation of junction normal resistances and cryogenic $E_J$ to be within ∼0.3% of design values across a device [35]. In addition, recent progress has been made in using normal metals [36] or low-gap superconductors [11], to suppress quasiparticle tunneling. These provide a pathway for the Josephson junction circulator to become practical technology for on-chip superconducting quantum processors.

In conclusion, we fabricated and characterized a passive superconducting circulator on a chip which is fully compatible with superconducting qubit fabrication and can be tuned with only dc control. We showed that the device circulation can be substantially improved by suppressing quasiparticle tunneling and reducing the disparity in the three Josephson junctions energies to 1% or less.

We thank Clemens Müller and Prasanna Pakkiam for useful discussions. This research was supported by the Australian Research Council Centres of Excellence for Engineered Quantum Systems (Project No. CE170100009).

---

[*] r.navarathna@uq.edu.au

[†] Present address: Department of Physics, ETH Zürich, CH-8093 Zürich, Switzerland.

[‡] a.fedorov@uq.edu.au

[1] D. Pozar, *Microwave Engineering* (Wiley, New York, 2011).

[2] X. Gu, A. F. Kockum, A. Miranowicz, Y. xi Liu, and F. Nori, Microwave photonics with superconducting quantum circuits, Phys. Rep. **718–719**, 1 (2017).

[3] A. Metelmann and A. A. Clerk, Nonreciprocal Photon Transmission and Amplification via Reservoir Engineering, Phys. Rev. X **5**, 021025 (2015).

[4] F. Ruesink, M.-A. Miri, A. Alù, and E. Verhagen, Nonreciprocity and magnetic-free isolation based on optomechanical interactions, Nat. Commun. **7**, 13662 (2016).

[5] A. Kord, D. L. Sounas, and A. Alù, Magnet-less circulators based on spatiotemporal modulation of bandstop filters in a delta topology, IEEE Trans. Microwave Theory Tech. **66**, 911 (2018).

[6] R. Fleury, D. L. Sounas, C. F. Sieck, M. R. Haberman, and A. Alù, Sound isolation and giant linear nonreciprocity in a compact acoustic circulator, Science **343**, 516 (2014).

[7] See Supplemental Material at http://link.aps.org/supplemental/10.1103/PhysRevLett.130.037001 for more details of the fabrication, experimental setup, charge noise, explanation of nonreciprocity, and simulations, fitting, and analysis of scattering matrix elements. The Supplemental Material includes Refs. [8–12].

[8] O. Cappé, E. Moulines, and T. Ryden, *Inference in Hidden Markov Models (Springer Series in Statistics)* (Springer-Verlag, Berlin, Heidelberg, 2005).

[9] L. A. Martinez, Y. J. Rosen, and J. L. DuBois, Improving qubit readout with hidden Markov models, Phys. Rev. A **102**, 062426 (2020).

[10] A. V. Dixit, S. Chakram, K. He, A. Agrawal, R. K. Naik, D. I. Schuster, and A. Chou, Searching for Dark Matter with a Superconducting Qubit, Phys. Rev. Lett. **126**, 141302 (2021).

[11] J. M. Martinis, Saving superconducting quantum processors from decay and correlated errors generated by gamma and cosmic rays, Quantum Inf. **7**, 90 (2021).

[12] J. Schreiber, Pomegranate: Fast and flexible probabilistic modeling in python, J. Mach. Learn. Res. **18**, 1 (2018), https://jmlr.org/papers/v18/17-636.html.

[13] B. J. Chapman, E. I. Rosenthal, J. Kerckhoff, B. A. Moores, L. R. Vale, J. A. B. Mates, G. C. Hilton, K. Lalumière, A. Blais, and K. W. Lehnert, Widely Tunable On-Chip Microwave Circulator for Superconducting Quantum Circuits, Phys. Rev. X **7**, 041043 (2017).

[14] A. Kamal, J. Clarke, and M. H. Devoret, Noiseless nonreciprocity in a parametric active device, Nat. Phys. **7**, 311 (2011).

[15] A. Kamal and A. Metelmann, Minimal Models for Nonreciprocal Amplification Using Biharmonic Drives, Phys. Rev. Appl. **7**, 034031 (2017).

[16] N. A. Estep, D. L. Sounas, J. Soric, and A. Alù, Magnetic-free non-reciprocity and isolation based on parametrically modulated coupled-resonator loops, Nat. Phys. **10**, 923 (2014).

[17] K. M. Sliwa, M. Hatridge, A. Narla, S. Shankar, L. Frunzio, R. J. Schoelkopf, and M. H. Devoret, Reconfigurable Josephson Circulator/Directional Amplifier, Phys. Rev. X **5**, 041020 (2015).

[18] F. Lecocq, L. Ranzani, G. A. Peterson, K. Cicak, R. W. Simmonds, J. D. Teufel, and J. Aumentado, Nonreciprocal Microwave Signal Processing with a Field-Programmable Josephson Amplifier, Phys. Rev. Appl. **7**, 024028 (2017).

[19] K. Fang, J. Luo, A. Metelmann, M. H. Matheny, F. Marquardt, A. A. Clerk, and O. Painter, Generalized nonreciprocity in an optomechanical circuit via synthetic magnetism and reservoir engineering, Nat. Phys. **13**, 465 (2017).

[20] C. W. Peterson, W. A. Benalcazar, M. Lin, T. L. Hughes, and G. Bahl, Strong Nonreciprocity in Modulated Resonator Chains through Synthetic Electric and Magnetic Fields, Phys. Rev. Lett. **123**, 063901 (2019).

[21] J. Kerckhoff, K. Lalumière, B. J. Chapman, A. Blais, and K. W. Lehnert, On-Chip Superconducting Microwave Circulator from Synthetic Rotation, Phys. Rev. Appl. **4**, 034002 (2015).

[22] P. Roushan *et al.*, Chiral ground-state currents of interacting photons in a synthetic magnetic field, Nat. Phys. **13**, 146 (2017).

[23] E. I. Rosenthal, B. J. Chapman, A. P. Higginbotham, J. Kerckhoff, and K. W. Lehnert, Breaking Lorentz

Reciprocity with Frequency Conversion and Delay, Phys. Rev. Lett. **119**, 147703 (2017).

[24] T. M. Stace, C. H. W. Barnes, and G. J. Milburn, Mesoscopic One-Way Channels for Quantum State Transfer via the Quantum Hall Effect, Phys. Rev. Lett. **93**, 126804 (2004).

[25] G. Viola and D. P. DiVincenzo, Hall Effect Gyrators and Circulators, Phys. Rev. X **4**, 021019 (2014).

[26] A. C. Mahoney, J. I. Colless, S. J. Pauka, J. M. Hornibrook, J. D. Watson, G. C. Gardner, M. J. Manfra, A. C. Doherty, and D. J. Reilly, On-Chip Microwave Quantum Hall Circulator, Phys. Rev. X **7**, 011007 (2017).

[27] Y.-X. Zhang, C. R. i Carceller, M. Kjaergaard, and A. S. Sørensen, Charge-Noise Insensitive Chiral Photonic Interface for Waveguide Circuit QED, Phys. Rev. Lett. **127**, 233601 (2021).

[28] J. Koch, A. A. Houck, K. L. Hur, and S. M. Girvin, Time-reversal-symmetry breaking in circuit-QED-based photon lattices, Phys. Rev. A **82**, 043811 (2010).

[29] C. Müller, S. Guan, N. Vogt, J. H. Cole, and T. M. Stace, Passive On-Chip Superconducting Circulator Using a Ring of Tunnel Junctions, Phys. Rev. Lett. **120**, 213602 (2018).

[30] V. Bouchiat, D. Vion, P. Joyez, D. Esteve, and M. H. Devoret, Quantum coherence with a single Cooper pair, Phys. Scr. **T76**, 165 (1998).

[31] J. Koch, T. M. Yu, J. Gambetta, A. A. Houck, D. I. Schuster, J. Majer, A. Blais, M. H. Devoret, S. M. Girvin, and R. J. Schoelkopf, Charge-insensitive qubit design derived from the Cooper pair box, Phys. Rev. A **76**, 042319 (2007).

[32] D. T. Le, C. Müller, R. Navarathna, A. Fedorov, and T. M. Stace, Operating a passive on-chip superconducting circulator: Device control and quasiparticle effects, Phys. Rev. Res. **3**, 043211 (2021).

[33] C. Caloz, A. Alù, S. Tretyakov, D. Sounas, K. Achouri, and Z.-L. Deck-Léger, Electromagnetic Nonreciprocity, Phys. Rev. Appl. **10**, 047001 (2018).

[34] M. Scheucher, A. Hilico, E. Will, J. Volz, and A. Rauschenbeutel, Quantum optical circulator controlled by a single chirally coupled atom, Science **354**, 1577 (2016).

[35] J. B. Hertzberg, E. J. Zhang, S. Rosenblatt, E. Magesan, J. A. Smolin, J.-B. Yau, V. P. Adiga, M. Sandberg, M. Brink, J. M. Chow, and J. S. Orcutt, Laser-annealing Josephson junctions for yielding scaled-up superconducting quantum processors, Quantum Inf. **7**, 129 (2021).

[36] E. T. Mannila, P. Samuelsson, S. Simbierowicz, J. T. Peltonen, V. Vesterinen, L. Grönberg, J. Hassel, V. F. Maisi, and J. P. Pekola, A superconductor free of quasiparticles for seconds, Nat. Phys. **18**, 145 (2022).